Growth of centimeter-scale multilayer hexagonal boron nitride films by metal-boride-vapor CVD

Jiawen Liu,[a, b] Yanping Sui,[a, b] Chenxi Liu,[a, b] Xiaolong Ming,[c] Chuang Tian,[a, b] Runhan Xiao,[a, b] Jie Cheng,[a, b] Yangjian Xu,[a, b] Haomin Wang,[a, b] Shujie Tang,[a, b] Haidi Wang,[c] Guanghui Yu * [d]

a. *State Key Laboratory of Integrated Circuit Materials, Shanghai Institute of Microsystem and Information Technology, Chinese Academy of Sciences, Shanghai 200050, China*
b. *Center of Materials Science and Optoelectronics Engineering, University of Chinese Academy of Sciences, Beijing 100049, China*
c. *School of Physics, Hefei University of Technology, Hefei, Anhui 230009, China*
d. *School of Integrated Circuits, Dongguan University of Technology, Dongguan 523808, China*

*Correspondence: ghyu@mail.sim.ac.cn

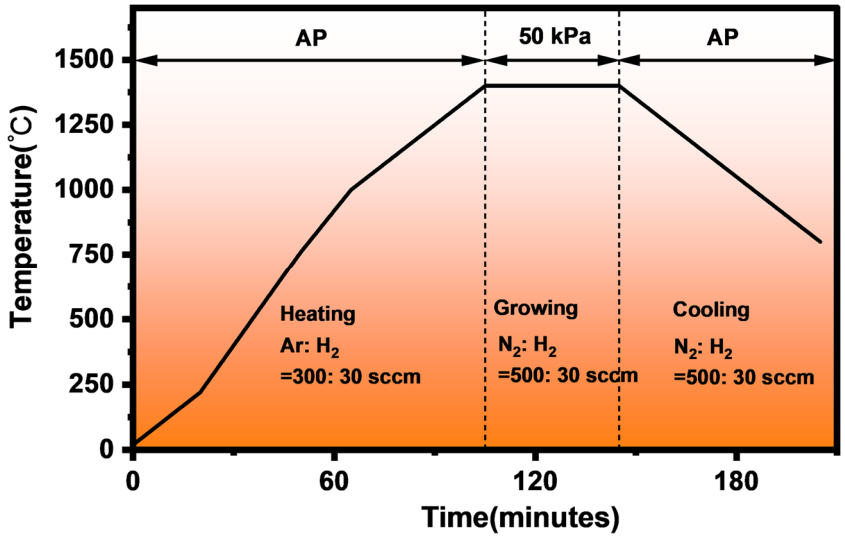

Fig S1. The schematic illustrates the conditions employed during the CVD process in this work. Under an Ar/H_2 atmosphere, the system was heated to 1400 °C, after which the pressure was reduced to 50 kPa and the atmosphere was switched to an N_2/H_2 mixture to ensure uniform distribution of nitrogen and boron sources. After a 30 min growth period, the pressure was restored to atmospheric pressure and the system was cooled down to room temperature.

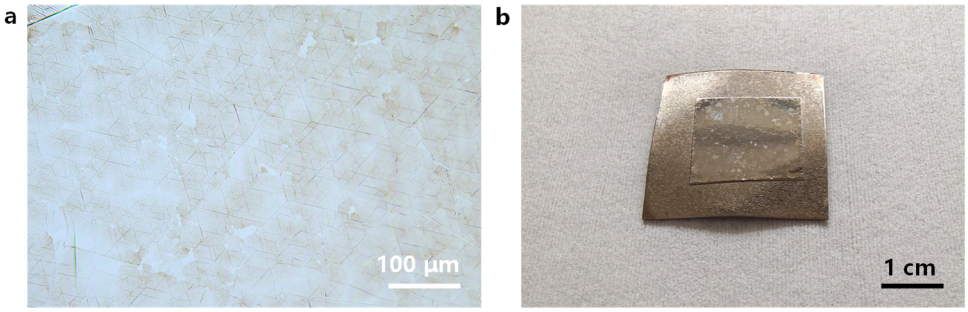

Fig S2. The boron sources prepared at 1150°C (a) and 1300°C (b) are used to grow *h*-BN films.

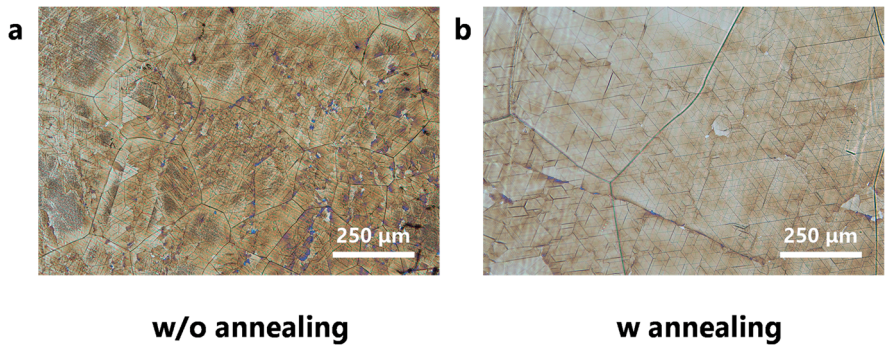

Fig S3. Critical role of substrate pre-annealing. Morphologies of *h*-BN grown by metal boride vapor CVD on (a) an as-received substrate and (b) a pre-annealed substrate, highlighting the effect of thermal pretreatment. The pre-annealed substrate provides a thermally stable surface at 1400 °C, facilitating continuous *h*-BN film growth. Conversely, the as-received substrate experiences recovery, recrystallization, and grain growth at high temperature, which prevents the formation of *h*-BN films.

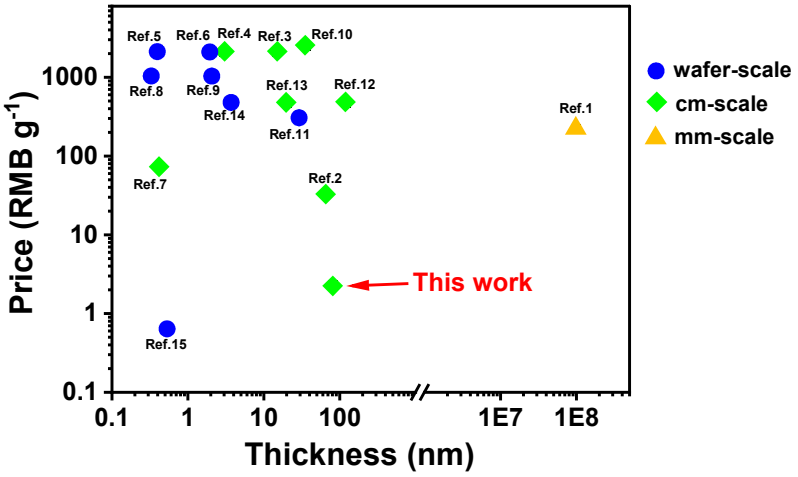

Fig S4. Thickness–primary precursor cost plot for representative *h*-BN film growth methods. For studies in which the precursor supplier is not explicitly specified, the average price from multiple suppliers is used. (Some price information is taken from *Small Methods*, 2025, **9**, 2401422.)

Table S1. Price list of 3N–5N purity boron powders and Ba_3N_2 from major suppliers

Boron					
Brand	Product ID	Weight (g)	Purity (%)	Price (RMB)	Unit price (RMB g^{-1})
Adamas	80543DE	25	99.999%	3500	140
	80543CE	100	99.99%	6296	62.96
	80543HE	500	99.9%	5700	11.4
Aladdin	Aladdin#B579275-25g	25	99.99%	1958.9	78.356
	Aladdin#B105888-25g	25	99.9%	1299.9	51.996
Alfa	Alfa#012820-5g	5	99.999%	12569	2513.8
Goodfellow*	B-00-ST-000100	~31.01	99.6%	9509.9	306.67
Ba_3N_2					
Adamas	116249BC	5	99.9%	1098	219.6

All data obtained from tansoole website (www.tansoole.com) on Feburary 2, 2025.

* This information is obtained from the Goodfellow website (www.goodfellow.com), which is the precursor supplier referenced in Ref. 11.

Table S2. Representative studies on *h*-BN film growth summarized in Fig. S4

Primary precursor	Reference	Reference number
Ba_3N_2	*Nat. Mater.*, 2004, **3**, 404.	1
Fe_2B	*Nat. Commun.*, 2020, **11**, 849.	2
Borazine	*Nat. Commun.*, 2015, **6**, 8662.	3
	ACS Nano, 2018, **12**, 6236.	4
	Science, 2018, **362**, 817.	5
	Nature, 2022, **606**, 88.	6
Ammonia borane	*Nano Lett.*, 2012, **12**, 161.	7
	Nat. Mater., 2024, **23**, 1495.	8
	Mater. Today, 2025, **88**, 168.	9
Boron	*Nanoscale*, 2021, **13**, 11223.	10
	Small, 2023, **19**, 2301086.	11
	J. Electron. Mater., 2023, **52**, 4913.	12
	2D Mater., 2024, **11**, 035033.	13
	Sci. China Mater., DOI:10.1007/s40843-025-3862-x.	14
h-BN	*Small Methods*, 2025, **9**, 2401422.	15

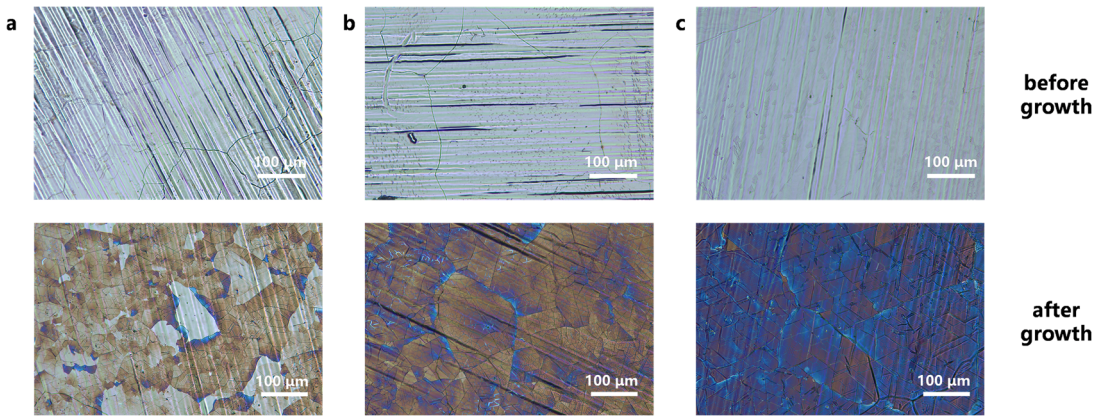

Fig S5. Boron segregation intensifies with increasing preparation temperature, as observed by optical microscopy. Images show the boron source before (upper) and after (lower) growth, prepared at (a) 1200 °C, (b) 1250 °C, and (c) 1300 °C. The polygonal features within the grains in the pristine sources are a result of boron segregation.

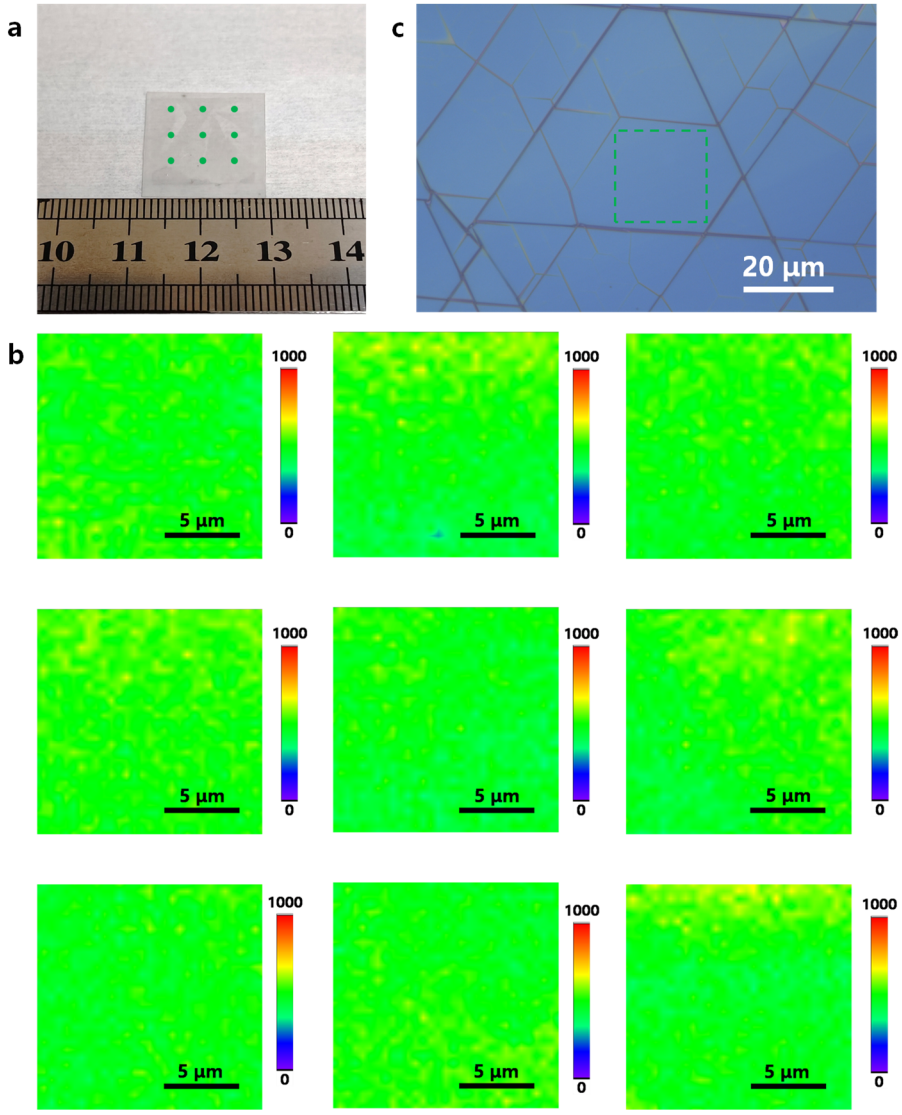

Fig S6. Raman mapping characterization of a transferred ~1.5 cm × 1.5 cm *h*-BN film grown using a boron source prepared at 1250 °C: (a) optical image of the *h*-BN/SiO2 (the black edge at the bottom of the film originates from the polymer residues in the transfer process); (b) integrated intensity of the E2g peak over 15 μm × 15 μm areas at nine positions corresponding to those marked in (a); (c) optical image of the *h*-BN/SiO2/Si corresponding to Fig 2c.

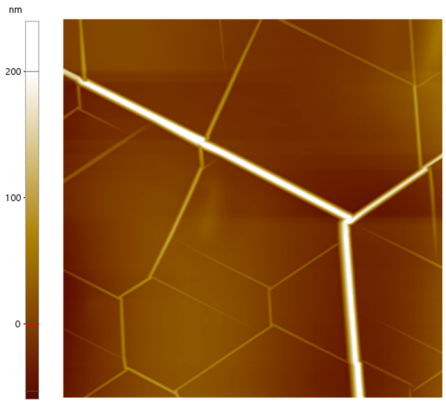

Fig S7. AFM image of the *h*-BN film grown by metal boride vapor CVD. Most wrinkles exhibit an angle of 120 °, with only a few showing 90 °, indicating that the wrinkles are well aligned along the armchair direction of *h*-BN.[13,16]

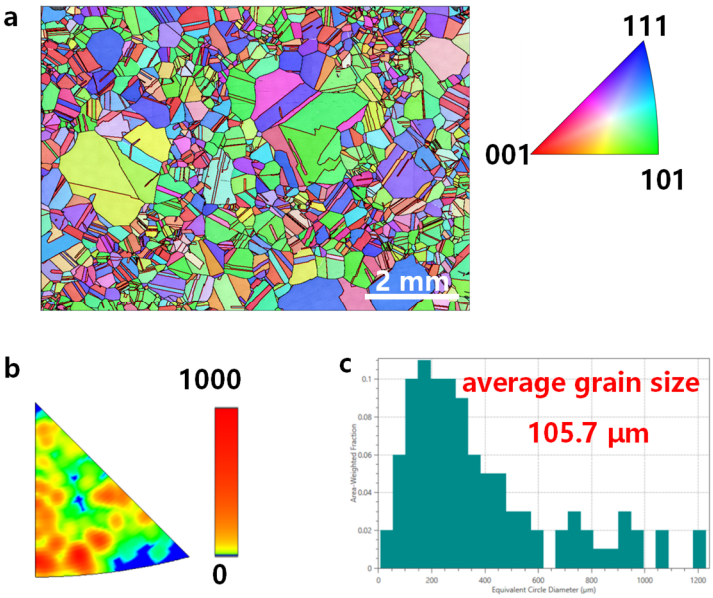

Fig S8. Grain characterization of a polycrystalline FeNi substrate annealed at 1430 °C for 3 h and used for *h*-BN growth: (a) IPF map obtained from EBSD characterization of an ~8.3 mm × 5.9 mm polycrystalline FeNi substrate; (b) distribution of facet indices of the IPFs along the normal direction in (a),which shows no (111) facet across an 8.3 mm × 5.9 mm polycrystalline FeNi substrate; (c)histogram of the equivalent circle diameter of grains within the region shown in (a).

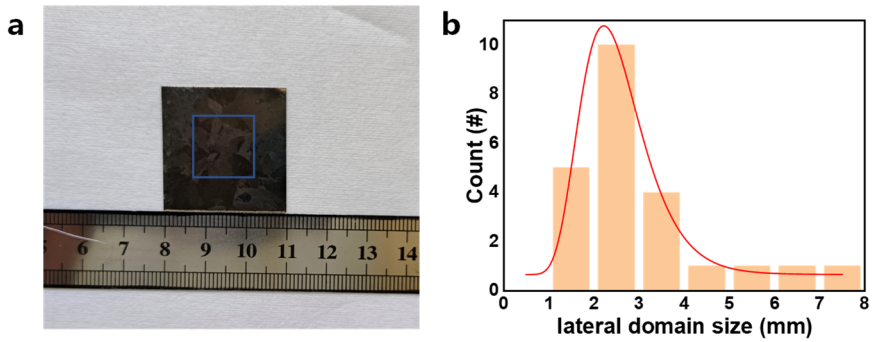

Fig S9. Statistical analysis of domain sizes within an ~1.5 cm × 1.5 cm area: (a) optical image of the sample used for the statistical analysis (the blue box indicates the analyzed region); (b) histogram of the lateral sizes of 23 domains within the analyzed region (the maximum lateral dimension of each domain is used), and the lateral size of *h*-BN domains is on the millimeter scale, exceeding the grain size of the FeNi substrate (see in Fig S8).

Table S3. Areas of the 23 domains within the analyzed region in Fig. S9a

	Domian area (mm^2)	Sum area/Total area
Domain area < 6 mm^2	0.97	~11.82%
	0.982	
	1.522	
	1.678	
	2.055	
	3.125	
	4.594	
	4.694	
	5.487	
Domain area > 6 mm^2	6.277	~88.18%
	6.449	
	6.524	
	6.625	
	7.478	
	8.453	
	9.484	
	10.954	
	11.761	
	16.017	
	18.46	
	19.406	
	21.19	
	38.269	

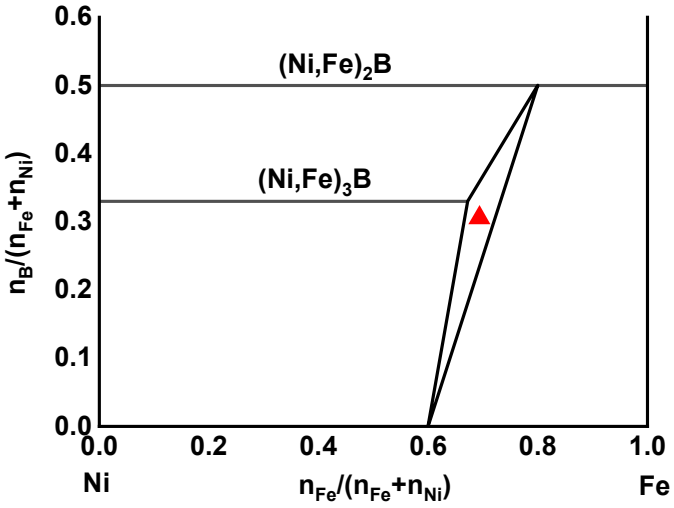

Fig S10. Fe–Ni–B ternary phase diagram at 925 °C. Reproduced with permission.[17]Copyright 2025, De Gruyter Brill.

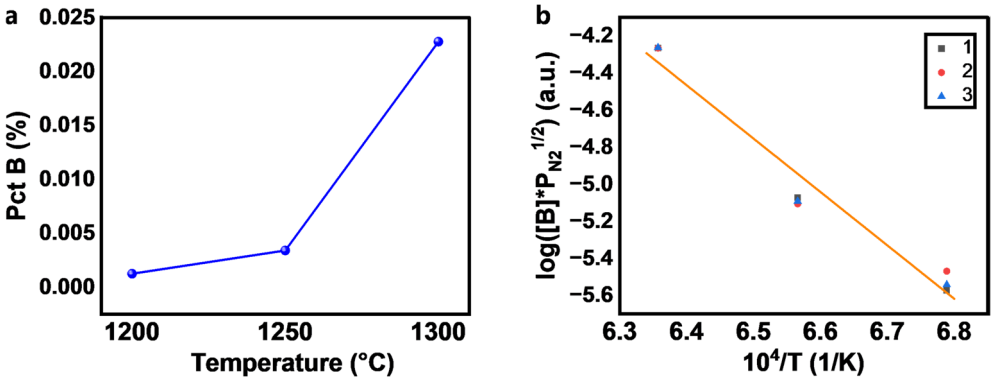

Fig S11. Boron content in boron sources prepared at different temperatures. (a) Variation of the boron mass fraction in the source with temperature during solid-state boronizing; (b) relationship between the equilibrium constant of BN = B + 1/2 N_2 and temperature. The plot of log([%B]×$P_{N2}^{1/2}$) versus 1/T shows good linearity, indicating that the boron concentration during solid-state boronizing has reached the equilibrium concentration under the corresponding conditions.[18]

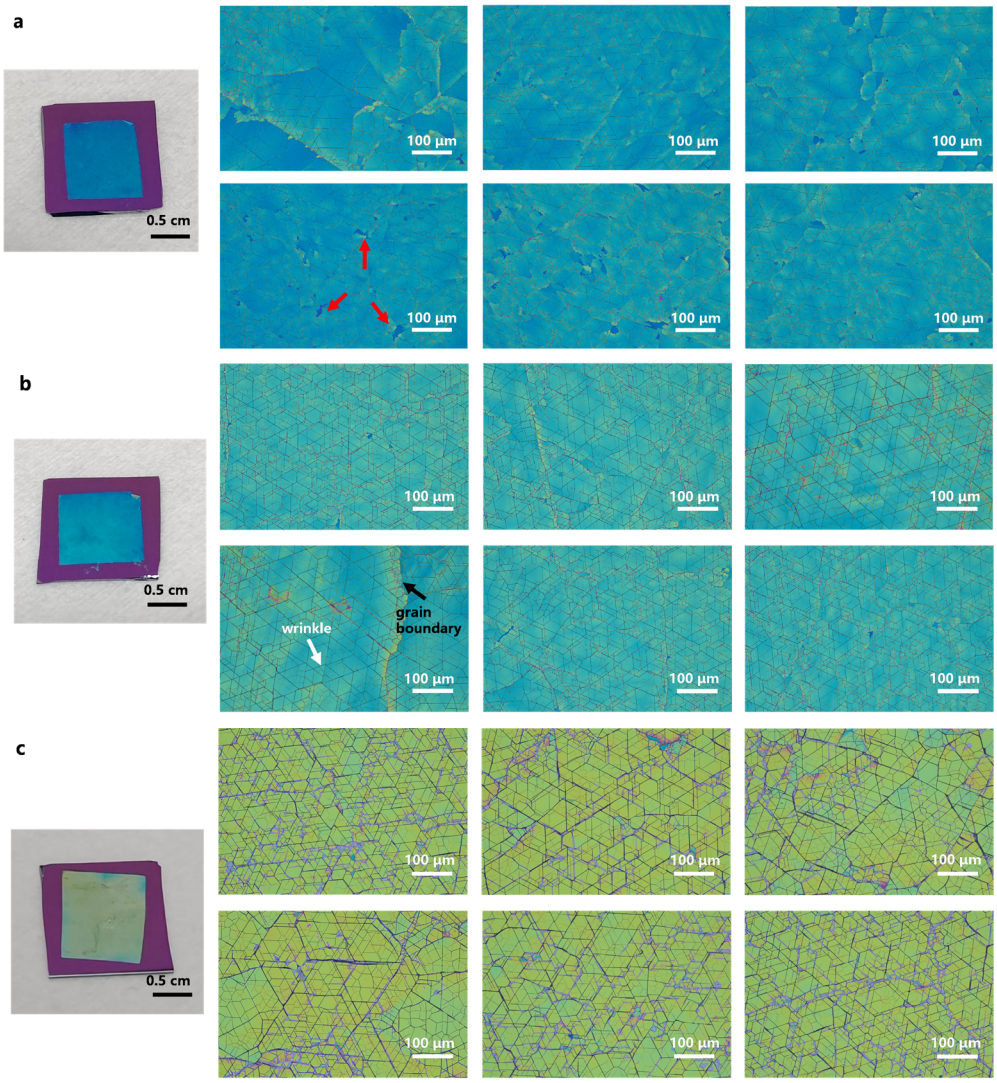

Fig S12. Optical micrographs of transferred *h*-BN films synthesized with boron sources obtained at varying boriding temperatures. Prior to transfer, the edges of all original substrates were trimmed. Images correspond to boriding temperatures of (a) 1200 °C, (b) 1250 °C, and (c) 1300 °C. (The regions indicated by red arrows in panel (a) correspond to pinhole-like regions, while the grain boundaries and wrinkles in the *h*-BN film are marked by black and white arrows, respectively, in panel (b). Moreover, the light purple networks visible in (c) represent bubbles at the *h*-BN/substrate interface.)

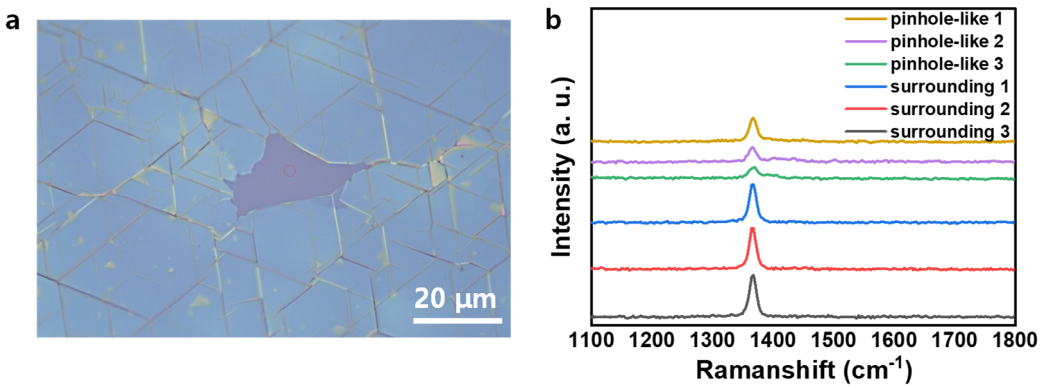

Fig S13. Characterization of pinhole-like regions in an *h*-BN film grown using a boron source prepared at 1200 °C: (a) optical microscope image of a representative pinhole-like region; (b) Raman characterization of three different pinhole-like regions and their surrounding areas.

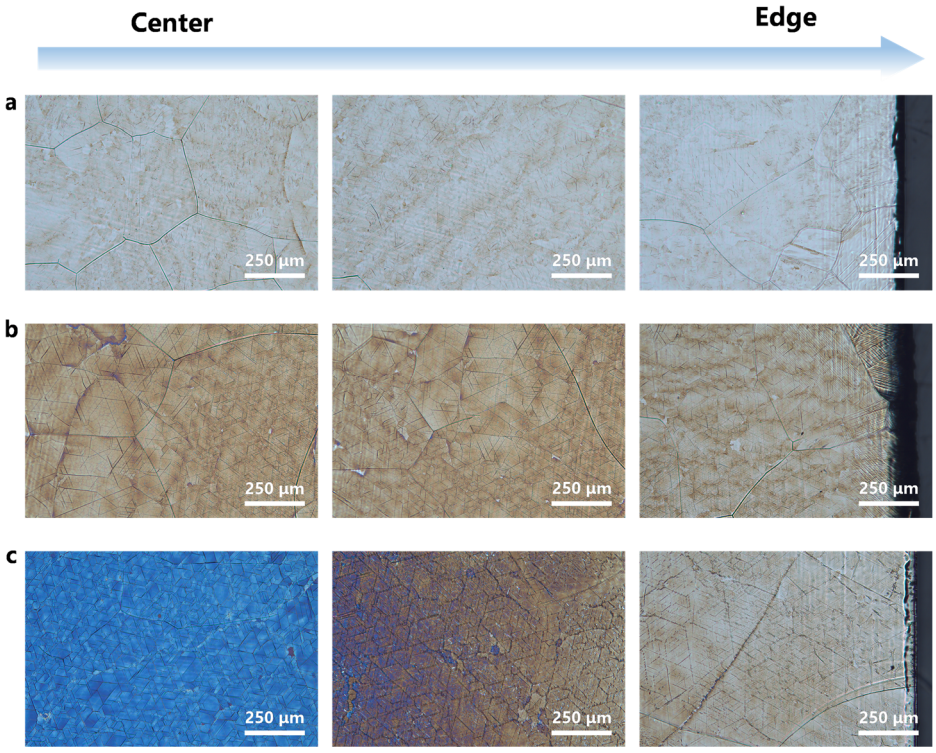

Fig S14. Uniformity of *h-BN* films grown on substrates with boron sources prepared at various temperatures: (a) 1200 °C, (b) 1250 °C, and (c) 1300 °C. The multilayer *h*-BN film in (c) exhibits a pronounced thickness gradient from the center to the edge of the substrate.

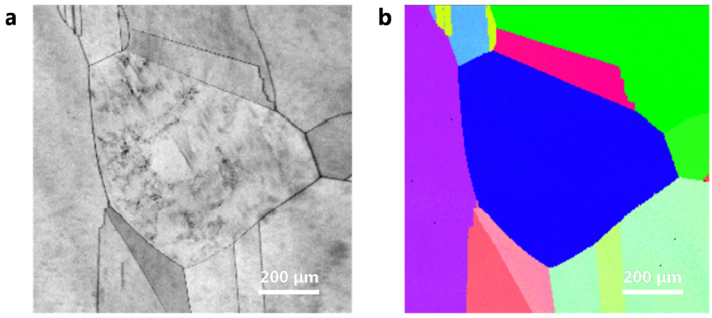

Fig S15. EBSD mapping over a larger area corresponding to the left region of Figure 5a. (a) Pattern quality, and (b) IPF map of EBSD measurement. The measurements were performed on the backside of the sample, as the front surface was covered by a thick *h*-BN film.

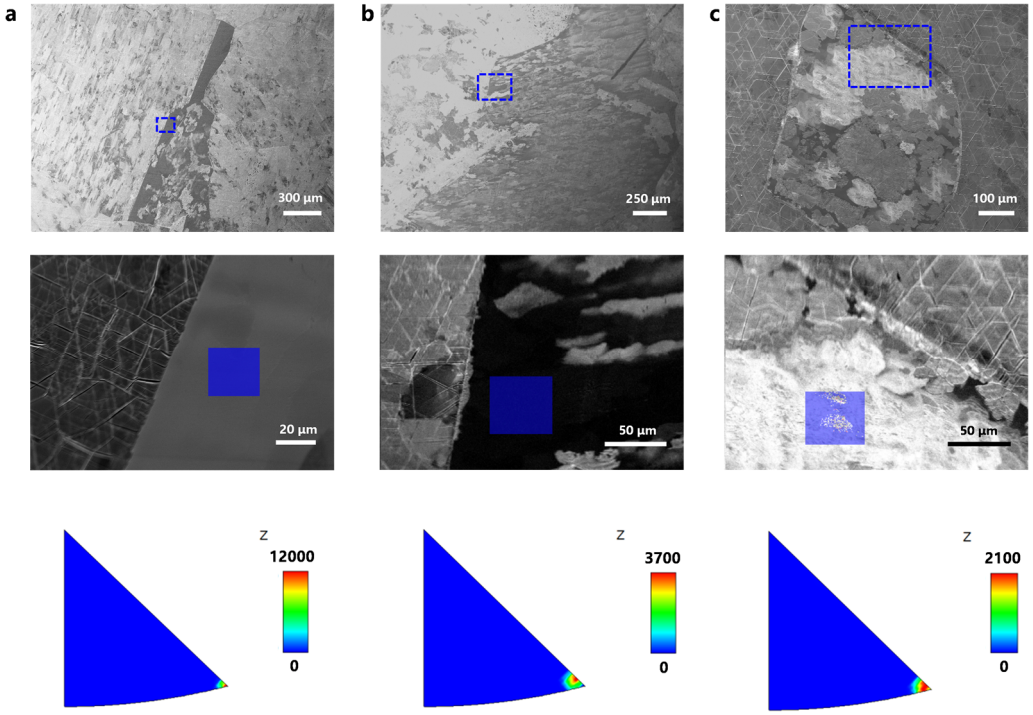

Fig S16. Growth of *h*-BN films on FeNi(111) grains using boron sources prepared at different boronizing temperatures: (a) 1200 °C, (b) 1250 °C, and (c) 1300 °C. The middle panel shows an enlarged view of the area demarcated by the blue rectangle in the upper panel.

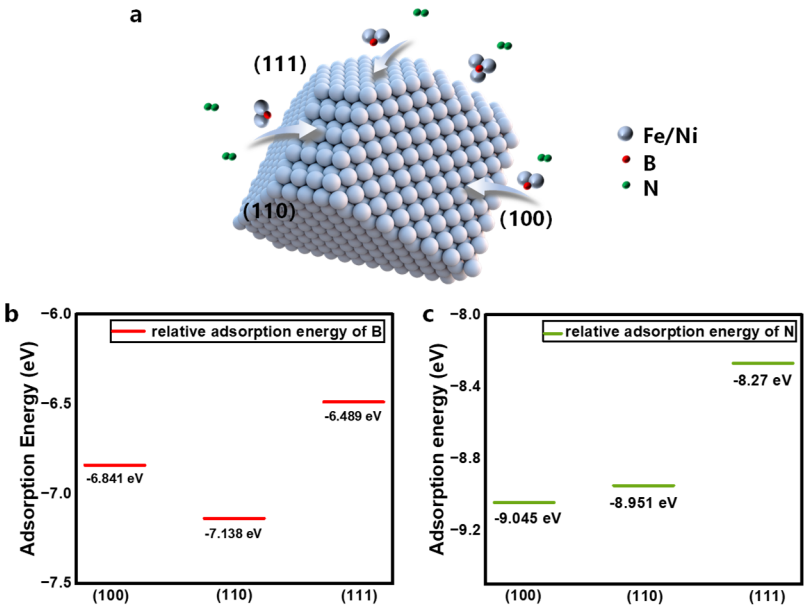

Fig S17. Calculated relative adsorption energies of B and N atoms on the (100), (110), and (111) surfaces of a FeNi alloy: (a) schematic illustration of B/N adsorption; (b) adsorption energies of B atoms; (c) adsorption energies of N atoms.

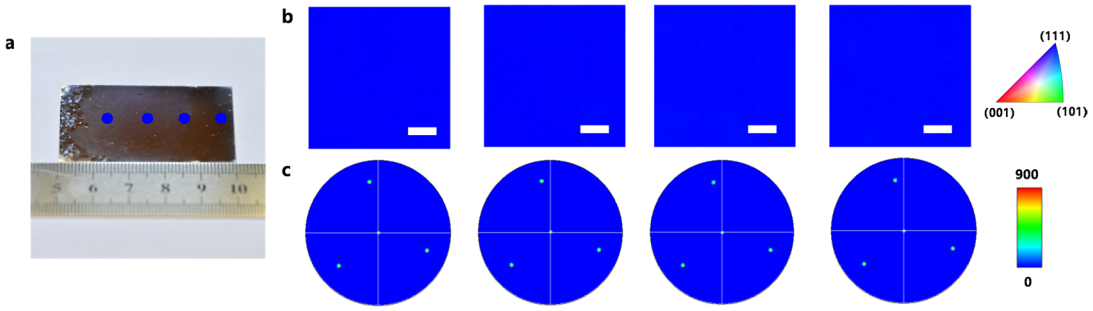

Fig S18. Preparation of FeNi(111) single crystal by high-temperature annealing.[19] (a) Optical image of the FeNi(111) single crystal (the bright region on the far left corresponds to a polycrystalline area); (b) EBSD IPF maps along the z-direction and (c) {111} pole figures obtained from the four points marked in (a). The scale bar in (b) is 20 μm.

Reference:

1 K. Watanabe, T. Taniguchi and H. Kanda, *Nat. Mater.*, 2004, **3**, 404–409.

2 Z. Shi, X. Wang, Q. Li, P. Yang, G. Lu, R. Jiang, H. Wang, C. Zhang, C. Cong, Z. Liu, T. Wu, H. Wang, Q. Yu and X. Xie, *Nat. Commun.*, 2020, **11**, 849.

3 S. M. Kim, A. Hsu, M. H. Park, S. H. Chae, S. J. Yun, J. S. Lee, D.-H. Cho, W. Fang, C. Lee, T. Palacios, M. Dresselhaus, K. K. Kim, Y. H. Lee and J. Kong, *Nat. Commun.*, 2015, **6**, 8662.

4 Y. Uchida, S. Nakandakari, K. Kawahara, S. Yamasaki, M. Mitsuhara and H. Ago, *ACS Nano*, 2018, **12**, 6236–6244.

5 J. S. Lee, S. H. Choi, S. J. Yun, Y. I. Kim, S. Boandoh, J.-H. Park, B. G. Shin, H. Ko, S. H. Lee, Y.-M. Kim, Y. H. Lee, K. K. Kim and S. M. Kim, *Science*, 2018, **362**, 817–821.

6 K. Y. Ma, L. Zhang, S. Jin, Y. Wang, S. I. Yoon, H. Hwang, J. Oh, D. S. Jeong, M. Wang, S. Chatterjee, G. Kim, A.-R. Jang, J. Yang, S. Ryu, H. Y. Jeong, R. S. Ruoff, M. Chhowalla, F. Ding and H. S. Shin, *Nature*, 2022, **606**, 88–93.

7 K. K. Kim, A. Hsu, X. Jia, S. M. Kim, Y. Shi, M. Hofmann, D. Nezich, J. F. Rodriguez-Nieva, M. Dresselhaus, T. Palacios and J. Kong, *Nano Lett.*, 2012, **12**, 161–166.

8 Y. Wang, C. Zhao, X. Gao, L. Zheng, J. Qian, X. Gao, J. Li, J. Tang, C. Tan, J. Wang, X. Zhu, J. Guo, Z. Liu, F. Ding and H. Peng, *Nat. Mater.*, 2024, **23**, 1495–1501.

9 X. Zhang, M. Dai, Y. Wu, Y. Hu, Q. Wang, S. Wang, H. Shang, B. Tan, Z. Su, Y. Ding, K. Liu, Y. Fu, J. Wang, P. Hu, D. Jia, Y. Zhou, L. Ling and X. Chen, *Mater. Today*, 2025, **88**, 168–177.

10 Y. Li, X. Wen, C. Tan, N. Li, R. Li, X. Huang, H. Tian, Z. Yao, P. Liao, S. Yu, S. Liu, Z. Li, J. Guo, Y. Huang, P. Gao, L. Wang, S. Bai and L. Liu, *Nanoscale*, 2021, **13**, 11223–11231.

11 G. Wang, J. Huang, S. Zhang, J. Meng, J. Chen, Y. Shi, J. Jiang, J. Li, Y. Cheng, L. Zeng, Z. Yin and X. Zhang, *Small*, 2023, **19**, 2301086.

12 D. Chen, H. Shen, B. Liu, Z. Wang, B. Liao, W. Mao, Y. Li and T. Wu, *J.*

Electron. Mater., 2023, **52**, 4913–4920.

13 Y. Zhu, Z. Shi, Y. Ruan and Q. Yu, *2D Mater.*, 2024, **11**, 035033.

14 N. Congcong, Q. Fangzhu, Z. Qinglong, G. Xiaomeng, Z. Hao, L. Jun, L. Jiawei, Z. Hongwei and L. Xuesong, *Sci. China Mater.*, DOI:10.1007/s40843-025-3862-x.

15 C. Chen, Q. Wang, Z. Zhang, Z. Liu, C. Xu and W. Ren, *Small Methods*, 2025, **9**, 2401422.

16 L. Chen, K. Elibol, H. Cai, C. Jiang, W. Shi, C. Chen, H. S. Wang, X. Wang, X. Mu, C. Li, K. Watanabe, T. Taniguchi, Y. Guo, J. C. Meyer and H. Wang, *2D Mater.*, 2021, **8**, 024001.

17 F. J. J. van Loo and J. A. van Beek, *Int. J. Mater. Res.*, 1989, **80**, 245.

18 R. W. Fountain and J. Chipman, *Trans. Metall. Soc. AIME*, 1962, **224**, 599.

19 J. Qi, C. Ma, Q. Guo, C. Ma, Z. Zhang, F. Liu, X. Shi, L. Wang, M. Xue, M. Wu, P. Gao, H. Hong, X. Wang, E. Wang, C. Liu and K. Liu, *Adv. Mater.*, 2024, **36,** 2303122.